ACS APPLIED MATERIALS & INTERFACES

Research Article

www.acsami.org

Design and Fabrication of a Hybrid Superhydrophobic–Hydrophilic Surface That Exhibits Stable Dropwise Condensation

Bikash Mondal,[†] Marc Mac Giolla Eain,[‡] QianFeng Xu,[§] Vanessa M. Egan,[‡] Jeff Punch,[‡] and Alan M. Lyons*[,†,§]

[†]Department of Chemistry, College of Staten Island and the Graduate Center, The City University of New York, Staten Island, New York 10314, United States

[‡]Stokes Laboratories, Department of Mechanical, Aeronautical & Biomedical Engineering, University of Limerick, Limerick, Ireland

[§]ARL Designs, New York, New York, United States

Supporting Information

ABSTRACT: Condensation of water vapor is an essential process in power generation, water collection, and thermal management. Dropwise condensation, where condensed droplets are removed from the surface before coalescing into a film, has been shown to increase the heat transfer efficiency and water collection ability of many surfaces. Numerous efforts have been made to create surfaces which can promote dropwise condensation, including superhydrophobic surfaces on which water droplets are highly mobile. However, the challenge with using such surfaces in condensing environments is that hydrophobic coatings can degrade and/or water droplets on superhydrophobic surfaces transition from the mobile Cassie to the wetted Wenzel state over time and condensation shifts to a less-effective filmwise mechanism. To meet the need for a heat-transfer surface that can maintain stable dropwise condensation, we designed and fabricated a hybrid superhydrophobic–hydrophilic surface. An array of hydrophilic needles, thermally connected to a heat sink, was forced through a robust superhydrophobic polymer film. Condensation occurs preferentially on the needle surface due to differences in wettability and temperature. As the droplet grows, the liquid drop on the needle remains in the Cassie state and does not wet the underlying superhydrophobic surface. The water collection rate on this surface was studied using different surface tilt angles, needle array pitch values, and needle heights. Water condensation rates on the hybrid surface were shown to be 4 times greater than for a planar copper surface and twice as large for silanized silicon or superhydrophobic surfaces without hydrophilic features. A convection–conduction heat transfer model was developed; predicted water condensation rates were in good agreement with experimental observations. This type of hybrid superhydrophobic–hydrophilic surface with a larger array of needles is low-cost, robust, and scalable and so could be used for heat transfer and water collection applications.

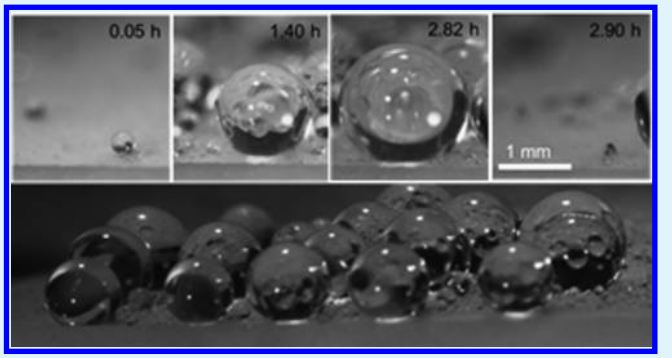

KEYWORDS: *dropwise condensation, hybrid superhydrophobic–hydrophilic, heat transfer, water collection, Cassie–Baxter, superhydrophobic surface*

1. INTRODUCTION

Condensation of water vapor is an important process for various applications such as heat transfer,[1−3] desalination,[4−6] and water collection[7−10] from the atmosphere. Heterogeneous condensation can occur on a solid surface in a dropwise and/or filmwise manner depending on the wettability of the condensing surface. Dropwise condensation (DWC) occurs when the condensed vapor forms as droplets on the condensing surface, which are removed relatively easily by sliding off under the force of gravity before coalescing into a film. DWC can lead to large increases in the heat transfer efficiency; some reports have indicated a 10-fold increase in heat transfer relative to film-wise condensation.[2,11,12]

Smooth hydrophobic surfaces have been modified to achieve DWC[2,12−23] using hydrophobic molecules such as alkylthiol,[12,18] alkylsilane,[11,24,25] or fluoropolymers.[19] Some of these coatings are sufficiently thin that no significant thermal resistance is introduced,[20] but the long-term durability of monolayer coatings remains a concern.[21] Polymer coatings on the surface can promote DWC but the coating thickness, which is necessary to ensure durability, contributes a substantial thermal resistance which offsets the advantage of DWC. Recently efforts have been made to make durable thin or

Received: July 24, 2015
Accepted: September 15, 2015

DOI: 10.1021/acsami.5b06759
ACS Appl. Mater. Interfaces XXXX, XXX, XXX−XXX

ultrathin polymer coatings by forming a stronger functional polymer and polymer−substrate bond using plasma-enhanced vapor[26] or initiated chemical vapor deposition (iCVD)[22] of hydrophobic polymers. Although a smooth hydrophobic surface can promote dropwise condensation with hemispherical droplet formation,[23] it can be difficult to maintain DWC if the droplet removal rate is slow.

Recently, wetting on various micro/nanostructured superhydrophobic (SH) surfaces have been reviewed[27] and investigated for studying DWC because of the enhanced droplet removal rates relative to smooth hydrophobic surfaces.[11,24−26,28−42] Depending on the surface geometry and roughness scale, water droplets formed during the condensation process could assume either the highly pinned Wenzel state (where liquid is in contact with a rough surface with no air layer separating liquid from solid) or the superhydrophobic Cassie−Baxter state, where the droplet can be easily shed from the surface at low tilt angles.[11,25,30,40,41] Superhydrophobic surfaces fabricated with two tier hierarchical surface roughness resulted in DWC under certain conditions;[35] however, the formation of a water film could also be observed.[31] DWC on nanostructured superhydrophobic silicon post surfaces has been observed with the formation of water droplets in the wetted (Wenzel), suspended (Cassie−Baxter), and partially wetted states. Heat transfer calculations showed that the partially wetted droplet could result in better heat transfer than suspended droplets due to the larger liquid−solid interface area.[25] Copper−copper oxide nanostructured SH surfaces showed a 25% higher overall heat flux compared to a hydrophobic copper surface. The heat transfer coefficient can be further improved on SH CuO surfaces by using an electric field assisted droplet removal process.[43] Another approach to increase heat transfer during DWC is to introduce high vapor shear forces that induce droplet movement across the surface even when the droplets partially wet the surface.[44] However, such surfaces degrade over time and transition to filmwise condensation.[44]

In addition to coating degradation, transitions from the Cassie to Wenzel state can occur due to condensation of water between surface features. Nucleation can occur equally in the regions between roughness features as on top of the roughness.[25,41,42] In this way, a SH surface could lose its superhydrophobicity and the condensed droplets would eventually wet the surface forming a continuous film of liquid.

To achieve better droplet mobility and stability, DWC on lubricant-infused micro/nanostructured surfaces has been studied.[45−47] Xiao et al.[46] demonstrated DWC with approximately 100% increase in heat transfer coefficient on oil-infused micro- and nanostructured CuO surfaces due to significantly increased nucleation density and facile condensate removal when compared to state-of-the-art DWC surfaces. Although this type of surface showed the potential for enhanced droplet removal, lubricant drainage over time could affect the long-term stability of the surface.

Another approach to achieving enhanced DWC is to fabricate a surface on which nucleation of water droplets can be directed to specific locations as demonstrated by the back of the Namib Desert beetle.[7,48−51] This natural hybrid hydrophobic−hydrophilic surface shows enhanced water collection by promoting DWC on raised hydrophilic regions. This phenomenon does not involve a heterogeneous condensation process as the fog already contains preformed condensed water droplets.[51] However, this type of natural surface provides a useful model to study dropwise condensation for applications including water collection[7−10] and heat transfer.[49,50,52] A hybrid hydrophobic/hydrophilic post surface can result in controlled condensation by preferentially promoting nucleation on the hydrophilic regions.[52] Recently a hybrid surface mimicking the beetle's back showed concurrent filmwise and dropwise condensation with 63% enhancement in heat transfer coefficient compared to a flat hydrophobic surface.[53]

Although these reports demonstrate that dropwise condensation on micro/nanostructured superhydrophobic and hybrid surfaces without wetting is possible,[25,31,54,55] long-term stability of condensation on these surfaces has not been demonstrated. In addition, many of these surfaces are fragile and difficult or expensive to fabricate. Thus, there is a need to prepare a reliable, robust surface which can promote dropwise condensation at high rates for long periods of time.

Here we present a simple, yet novel approach to fabricate a hybrid superhydrophobic−hydrophilic surface that exhibits stable dropwise condensation in high humidity environments. Inspired by the Namib Desert beetle elytra, we combine a superhydrophobic polymer surface that is highly abrasion resistant and can be fabricated in large areas for low cost, with an array of thermally interconnected hydrophilic steel needles, exploiting the wetting and thermal conductivity properties of each type of material on length scales comparable to that of the beetle.

To create the hybrid superhydrophobic−hydrophilic surface, an array of steel needles with high surface energy was soldered into a temperature controlled copper block. The needles are forced through a superhydrophobic polymer nanocomposite film with low surface energy such that the tips protrude a controlled amount. Nucleation occurs preferentially on the hydrophilic and cooler needle surface rather than the superhydrophobic and warmer polymer nanocomposite. As the droplet pinned on the needle grows, it contacts the underlying superhydrophobic polymer without wetting the surface. Once the droplet reaches a critical volume, gravity overcomes the triple contact line (TCL) forces between the water droplet and the needle, the droplet is released, and the droplet rolls off the surface. This droplet growth and roll-off process was monitored for more than 5 days without any indication of surface wetting. The condensation efficiency of the hybrid surface was studied by systematically adjusting tilt angles, needle height, needle pitch, and copper block temperature. Condensation rates were determined by quantifying water collected as well as by measuring droplet sizes before roll-off from the surface. Heat transfer from vapor to surface was calculated by measuring the temperature gradient across the steel needles. Condensation rates calculated from the heat transfer model were in good agreement with experimentally determined values.

2. EXPERIMENTAL SECTION

2.1. Surface Preparation. Superhydrophobic surfaces were prepared by laminating an ultrahigh molecular weight polyethylene film (120 μm thick, Saint Gobain Performance Plastics) against a layer of silica nanoparticles (CAB-O-SIL TS-530, a fumed silica and modified with hexamethyldisilazane, Cabot Corporation) at 177 °C under 70 MPa for 45−60 min. Excess particles were removed by rinsing the surface with water followed by ultrasonication of the film in water for 10 min.

Copper (alloy110, 99.9% Cu) was cut to size (20 × 20 × 4 mm) and cleaned by sonication in aqueous ammonium persulfate (Fisher Scientific) solution (30% w/v) at room temperature for 10 min. Methyl-terminated hydrophobic surfaces were prepared on polished

DOI: 10.1021/acsami.5b06759
ACS Appl. Mater. Interfaces XXXX, XXX, XXX−XXX

oxidized silicon substrates by a chemical vapor deposition (CVD) method. The silicon wafer was first cleaned in oxygen plasma (Plasma Preen II-973) for 45 s. The cleaned sample (CA < 5°) was placed into a jar fitted with a tube and stopcock for connection to a vacuum line. Approximately 2 mL of dichlorodimethylsilane (Sigma-Aldrich) was added and then vacuum was applied to the jar for 2 min to reduce the pressure to 70 kPa. Subsequently, the sealed jar was placed in an oven at 90 °C for 10 min and then kept at RT overnight. The prepared surface was rinsed with deionized water to remove excess reagent from the surface. A stable hydrophobic silicon surface was formed with a water contact angle (CA) of 102° and a slip angle of 3°.

2.2. Fabrication of Hybrid Superhydrophobic–Hydrophilic Surface. Hybrid superhydrophobic–hydrophilic surfaces were prepared by impaling a superhydrophobic film onto an array of steel needles (size 12 quilting needles, Piecemakers). The needles have a 500 μm shaft diameter tapering to an ~20 μm tip diameter. A detailed image of the needle is shown in the inset to Figure 1. To determine

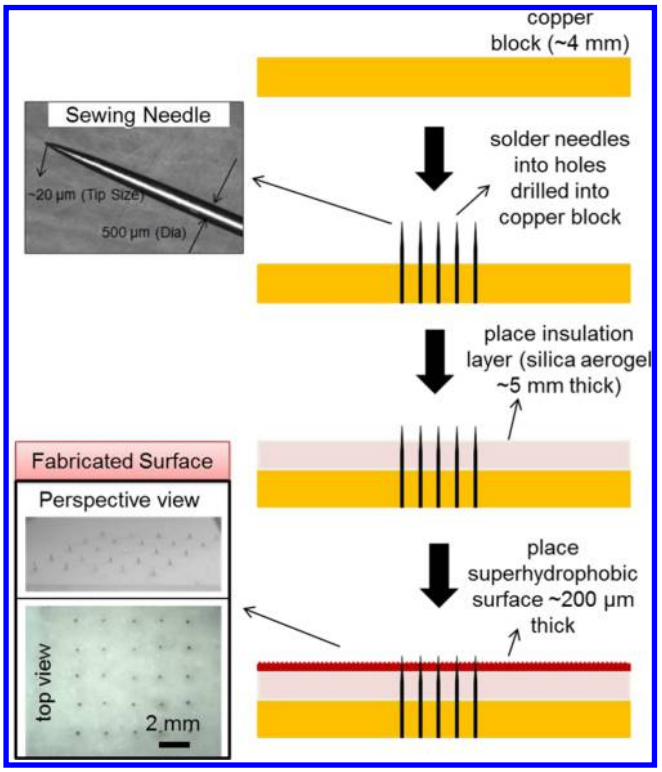

Figure 1. Schematic of the fabrication sequence for forming a hybrid superhydrophobic–hydrophilic surface, needle images (top, left) and a representative fabricated surface (bottom, left).

the contact angle of the needle, the CA of a flat steel substrate was measured using a 4 μL water droplet. The CA of water on flat steel was 77°. To form the needle array, a square array of 0.5 mm diameter through-holes was drilled into a 4 mm thick square (20 × 20 mm) copper block. The needle shafts were inserted into the holes and soldered in place with Sn–Pb solder. The backside was sanded to remove excess solder and form a smooth, flat surface. Once the needles were assembled into the copper block, a layer of thermal insulation material (Aspen Aerogel, ~5 mm thick) was pressed down through the needles. The prepared superhydrophobic surface was then pressed through the needles as shown schematically in Figure 1. The polymer substrate was pierced by the needles ensuring a good seal between needle and surface. To maintain a specific needle height above the superhydrophobic surface, a glass slide with Kapton tape shims of the desired thickness was used as a spacer. In this way, the polymer substrate was pierced with needles to the height determined by the thickness of the tape. A series of hybrid surfaces with 5 × 5 needle arrays on pitches ranging from 1 to 3 mm was fabricated.

2.3. Characterization of Superhydrophobic Surfaces. The surface structures were studied by field emission scanning electron microscopy (FE SEM, Amary 1910) and optical microscopy (Nikon-SMZ 1500). The static contact angles (CAs) and roll-off angles were measured with a goniometer (250-F1, ramé-hart Instrument Co.) at room temperature and pressure using distilled water. Droplet volumes of 2–5 and 10 μL were used to measure CA and roll-off/slip angle, respectively.

2.4. Condensation Experiment. Condensation studies were performed in a Delrin condensation chamber, specially built for these experiments, as shown schematically in Figure 2. The cylindrical chamber dimensions are as follows: inner diameter, 100 mm; depth, 60 mm; and wall thickness, 25 mm. The top of the chamber was sealed with a glass window that was fitted with an O-ring seal. An aluminum cooling stage was mounted into the base of the chamber, also with an O-ring seal. A fluid channel was drilled through the cooling stage and compression fittings were attached enabling the flow of chilled fluid to maintain the base at a constant temperature. The temperature of the fluid was maintained with a chiller (NESLAB RTE-740, Thermo Scientific). The substrate to be tested was placed onto the cooling stage using a thin layer of thermal grease.

To create a flow of humid air through the chamber, a stream of dry air (at a 10 psi delivery pressure, flow rate of 50 cc/min) was introduced to a heated water bubbler maintained at 80 °C to saturate the air stream before entering the condensation chamber. The humid air entered on one side of the chamber and exited on the opposite side through compression fittings to ensure airtight seals. To maintain a constant pressure within the chamber, and exclude dry air from entering, the outlet of the condensation chamber passed through a silicone oil bubbler to maintain a constant back pressure of 95 Pa. The relative humidity (RH) and air temperature of the chamber was monitored using a Traceable Hygrometer, Thermometer, Dew point probe (model 4085 Control Company) using a compression fitting mounted through the wall of the Delrin chamber. The probe was positioned 20 mm above the condensation surface in the center of the chamber.

The temperature of the condensing surface was monitored using a precision fine wire thermocouple (CHL-005, 127 μm diameter) or sheathed thermocouple (CHQSS-020G-6 508 μm diameter sheath) purchased from Omega Engineering Inc. The thermocouples were inserted through a rubber septum that was fitted into a hole drilled through the chamber wall. By bending the wires or sheath, the thermocouple could be held in contact with either the needle tip or SH surface through the spring force of the wire. Temperature values were recorded with the chamber closed and maintained at operating conditions. The tilt of the condensing surface was adjusted by tilting the chamber at a specific angle relative to the horizontal. Images of the condensation process were acquired with using a Nikon-SMZ 1500 (1× objective) stereo microscope equipped with an Infinity-2 digital camera at preset time intervals (1 to 5 min) and then analyzed using ImagePro7 software.

2.5. Test Sequence. To evaluate the condensation rate, a hybrid surface was placed on the cold plate using grease as a thermal interface material and the chamber was sealed. Dry air was purged through the chamber (200 mL/min for 45 min) during which time the chiller was set to the specified value (typically 5 °C). Upon reaching a stable temperature, the air flow was reduced (25–50 mL/min) and switched from the dry air source to the preheated water bubbler to introduce the humidified air flow. The introduction of humid air was defined as the starting time for the condensation observations.

2.6. Determination of Water Collection Rate. The water that condensed and rolled-off the surface was quantified by two techniques: weighing the collected water and optical measurements of the diameter of the droplets immediately before roll-off. To collect the water that condensed and rolled-off the surface, a superhydrophobic funnel was fabricated such that water rolling off the hybrid surface was directed into a vial.

The superhydrophobic funnel was made from the same material as the test surface and subsequently cut and folded into the shape of a funnel (Figure S1a). The funnel was placed under the condensation

DOI: 10.1021/acsami.5b06759
ACS Appl. Mater. Interfaces XXXX, XXX, XXX–XXX

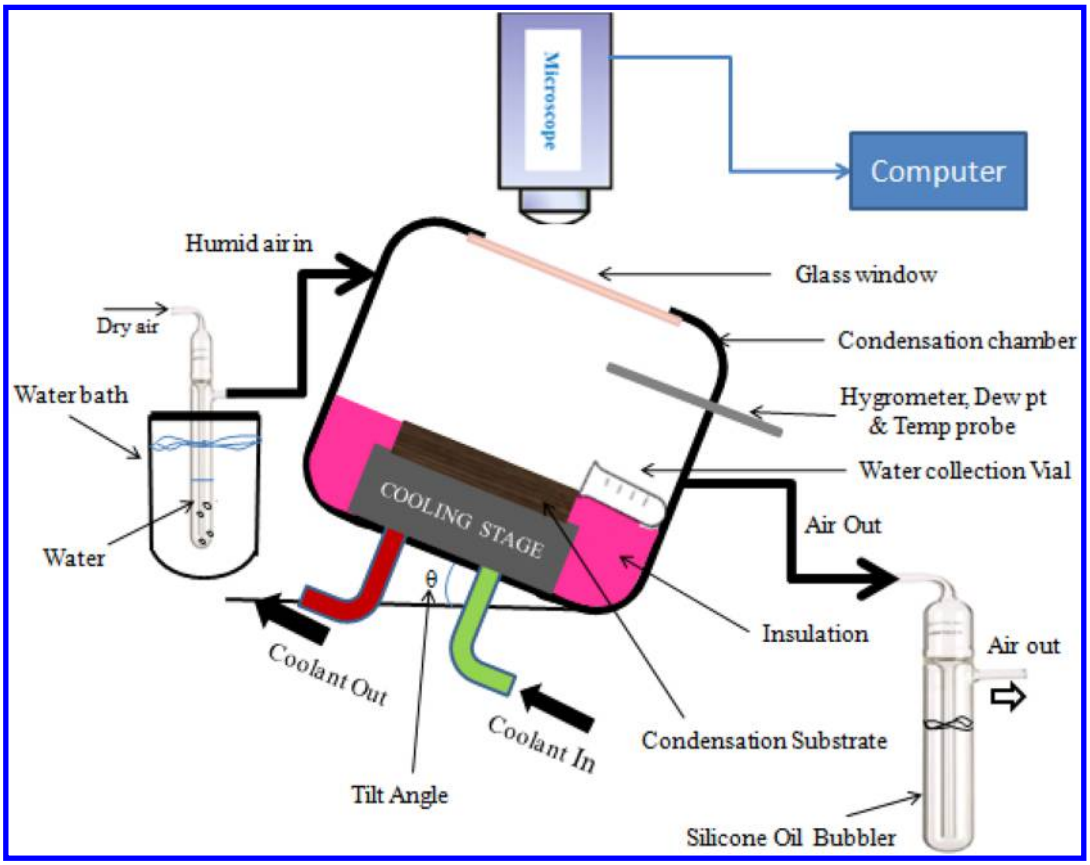

Figure 2. Experimental set-up for condensation study.

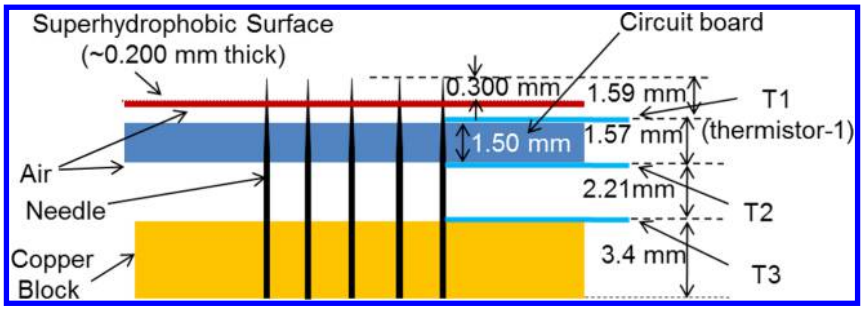

Figure 3. Schematic of needle array with an isothermal FR-4 laminate attached to facilitate the measurement of the needle temperature (cross-sectional view).

substrate to collect the water and direct it into the vial (1.8 mL, CryoTube Vial, Nunc) as shown in Figure S1b. Water collection rates were calculated by weighing the water collected in the vial over the full length of the experiment and dividing by the total time as well as the area of the condensing surface area (100 mm^2 for a 5 × 5 array on 2 mm pitch).

A second method to determine condensed water volume was based on calculating the volume of droplets measured by optical microscopy. The droplet diameter was measured in the last image recorded before roll-off, and the volume was calculated assuming a perfectly spherical drop shape. Images were typically recorded from looking down onto the substrate as shown in Figure S2 unless otherwise indicated. Thus, total water roll-off volume or mass was calculated by summing all droplets over the entire course of the condensation study.

2.7. Heat Transfer Study. To investigate dropwise condensation heat transfer rates on the hybrid superhydrophobic surface, local surface temperature measurements were recorded using a series of three thermistors (Betatherm glass bead fast response thermistors, model G22K7MCD419, 2 mm in length and 0.38 mm in diameter with a nominal resistance of 22 kΩ at 25 °C). These thermistors were chosen for their high temperature sensitivity and small size which also allowed both thermal and spatial uncertainties to be kept to a minimum, thereby minimizing the overall uncertainties in the inferred tip temperature. The thermistors were placed precisely along the length of the needle at distances of 1.52, 3.09, and 5.30 mm from the needle tip as shown in Figure 3 and Figure S3). As the diameter of the needle tip is 0.020 mm, it was not possible to attach the thermistors directly to the tip surface. Consequently, the tip temperature was extrapolated from the three thermistor values. Thermistor resistances were measured using a LakeShore 370 AC resistance bridge equipped with a 16-channel scanner to provide accurate and precise four wire resistance measurements. An excitation current of 31.6 nA was used to minimize thermistor self-heating. The thermistors were calibrated using a Thermo Scientific NESLAB RTE740 calibration bath over the temperature range of 0−35°C to reduce the uncertainty in the resistance readings.

Due to the curved surface of the needle and the flat surface of the sensing element, the thermistors could not be attached directly to the needle surface while maintaining good thermal contact. Consequently, a series of highly conductive metal planes (FR-4 PWB laminate),

DOI: 10.1021/acsami.5b06759
ACS Appl. Mater. Interfaces XXXX, XXX, XXX−XXX

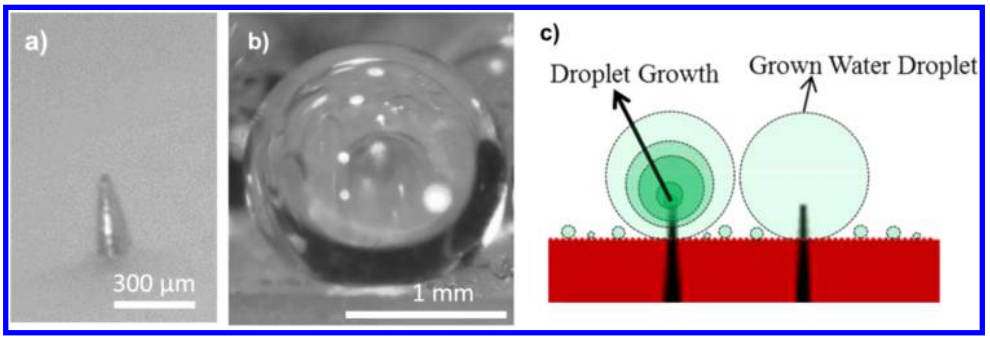

Figure 4. Condensation on a hybrid surface (a) a single needle before condensation begins. (b) Side view of a single drop and (c) a schematic of droplet growth due to preferential nucleation and droplet growth on the hydrophilic needle.

consisting of a copper alloy, $k \sim 400$ W/mK, were attached to the needle, as shown in Figure 3 and Figure S3. As a consequence of their high thermal conductivity, when brought into contact with the needle surface, the sheets reach the same temperature as the needle. These planes acted to support the thermistors, allowing them to be securely attached to the needle surface. The thermistors were bonded to both the isothermal surfaces and the needle using a thin layer of Loctite 489 adhesive.

Data Reduction. Three thermistor readings were used to measure the temperature gradient along the needle. The needle tip temperature was inferred from a linear extrapolation of the thermistor readings and hence used in the calculation of an effective heat transfer coefficient and condensation rate. These measurements were also used to determine the heat dissipated by the condensate to the needle (i.e., calorimeter). The heat dissipated along the needle (Q) was calculated using Fourier's Law of heat conduction:

$$Q = k\overline{A_{CS}}\frac{\Delta T}{\Delta x} \quad (1)$$

where k is the thermal conductivity of the needle, $\overline{A_{CS}}$ is the needle average cross sectional area, and $\Delta T/\Delta x$ is the spatial gradient of temperature along the needle. A needle average cross-sectional area 4.4 $\times 10^{-2}$ mm^2 was used as the needle diameter varies from 0.020 mm at the tip to 0.5 mm at the base.

The effective heat transfer coefficient between the vapor and needle tip (h_{eff}) was calculated by

$$h_{eff} = \frac{Q}{A_{exp}(T_{dew} - T_{tip})} \quad (2)$$

where T_{dew} is the dew point temperature, T_{tip} is the needle tip temperature, and A_{exp} is the surface area of the needle that is exposed to the saturated vapor mixture.

3. RESULTS AND DISCUSSION

3.1. Characterization of the Superhydrophobic (SH) and Hybrid Superhydrophobic–Hydrophilic Surfaces. The superhydrophobic (SH) surface is composed of silica nanoparticles partially embedded into the polyethylene substrate forming a surface with hierarchical roughness. The roughness results from the primary silica particle size (20 nm) as well as agglomerates of these silica nanoparticles (100–200 nm in diameter) as shown in SEM images in Figure S4. The static contact angle and slip angle of the SH background surface (Figure S4b inset) were measured to be 168 ± 2° and 2°, respectively. The hybrid superhydrophobic–hydrophilic surface (hybrid surface) surface exhibited a similar static contact angle when a drop was formed on the needle. The slip angle of a droplet pinned on the tip of the needle, however, increased to 21° when the height of the needle was 300 μm above the SH surface. The higher slip angle (21° vs 2°) results from the longer TCL which forms along the liquid–steel interface as well as the relatively low receding contact angle of water on the hydrophilic steel surface. An increase in slip angle with lengthening TCL was similarly observed when droplets wet the sides of sloped posts of polydimethylsiloxane.[56]

3.2. Sustained Dropwise Condensation on the Hybrid Surface. Figure 4 shows DWC on a hybrid surface due to condensation of water vapor on it. A single needle, before the start of condensation is shown in Figure 4a. Water condenses on the needles during the experiment forming nearly spherical droplets that remain in the Cassie state (CA ~168°) as shown in Figure 4b. The DWC on the hybrid surface was observed due to preferential nucleation and droplet growth on the needle tip as shown schematically in Figure 4c. A time-lapse video of a condensation experiment with a hybrid superhydrophobic–hydrophilic surface (5 × 5 needle array, tilting downward from right to left at a 33° angle, interval between images: 5 min, total elapsed time 20.3 h) is shown in Movie 1.

Continuous DWC on the hybrid surface was observed over the course of 28 h as seen from the images in Figure 5 (movie of an experiment run for 18 h can be found in Movie 2). Once humid air was introduced into the chamber, condensation was observed to selectively occur on the cooler, hydrophilic needle surfaces (temperature of the needle was 10 °C, whereas background SH surface was 12 °C) as shown in Figure 5a. This selective condensation is consistent with predictions based on the effect of surface energy on droplet nucleation rates. The high nucleation rate on the needle surface and relatively sparse nucleation of droplets on the SH surface are apparent in Figure 5 (panels a and c) and 6. The preferential nucleation on the hydrophilic needle surface (CA ~ 77°) rather than the superhydrophobic polyethylene nanocomposite surface (CA ~ 105°) is calculated to be 10^{49} using the equation from ref 52 (see Section 1 of the Supporting Information). Although this value is very high, it is significantly lower than the enhanced nucleation value, 10^{129}, reported for hydrophilic silica over hydrophobic silica.[52] The 2 °C lower temperature of the needle also enhances preferential nucleation on the needle surface. Since the condensation of water is an exothermic process, heat released during condensation must be dissipated to maintain the temperature of the liquid below the dew point in the chamber. For droplets pinned on needles, heat is transported from the liquid surface, across the drop, and through the needle to the heat sink. For droplets that randomly nucleate on the SH substrate, heat can only be conducted through the insulating SH surface and so will be dissipated more slowly. Over the course of the experiment, the temperature of these isolated droplets is expected to increase and so their relative growth rate slows over time due to relative preference for evaporation. The

DOI: 10.1021/acsami.5b06759
ACS Appl. Mater. Interfaces XXXX, XXX, XXX–XXX

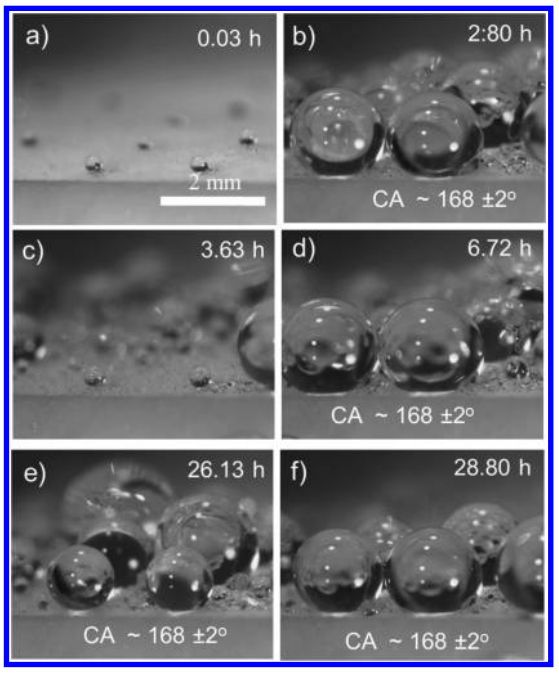

Figure 5. Optical microscope images during condensation showing the growth and release of droplets over 28.8 h, where droplets maintained a superhydrophobic Cassie state throughout: (a) preferential nucleation and droplet growth on the needle array observed 0.03 h (or 2 min) after introduction of moist air, (b) fully grown droplet array just before roll-off, (c) starting a second cycle of droplet nucleation after 3.63 h, (d) cycle 2 just before roll-off after 6.72 h total elapsed time, and (e and f) droplets after more than 26 and 28 h demonstrating long-term stability of superhydrophobicity (RH, 68 ± 2%; cooling stage temp, 5 °C; surface temp, 10 °C for needles and 12 °C for PE-SH surface; surface tilt angle, 22°).

sparse nucleation on the SH surface and the slow rate of growth of these droplets can be seen in Figures 5 and 6.

The growth of droplets on the needle tips proceeds not only by condensation of vapor but also through the merging of the satellite droplets formed on the background SH surface which have either rolled into the pinned droplet or have been imbibed by the growing droplet.

Figure 6 shows a series of optical images at 1 h time intervals during a condensation experiment which covers one full cycle of nucleation, droplet growth, and roll-off. Initially (2 min after onset), water is condensed onto the needle tips. After 1 h, spherical droplets, 0.869 ± 0.063 mm diameter, are easily observed in the optical microscope images. As the droplets continue to grow, the spherical droplet shape and CA of 168 ± 2° is maintained (Figure 6, panels b–g). The growth rate of the droplets pinned on the needles is 0.25 mg/h or 4.2×10^{-3} mg/min as determined by measuring the increase in droplet volume. Most droplets rolled off from the surface between 5.28 and 5.53 h of elapsed time. A sequence of photos taken during a separate experiment is shown in Figure S2; images were recorded at 5 min intervals.

To initiate roll-off, the droplet must reach a critical volume, above which gravity is sufficient to overcome the forces acting at the TCL, which allows the pinned droplet to begin rolling downslope toward the funnel. As the droplet rolls downward, all droplets in its path, both those droplets pinned on needle tips as well as smaller droplets nucleated on the SH surface, merge with the moving droplet and are carried away leaving a swath free of condensate (Figure 6h and Figure S2). After roll-off, water continues to condense preferentially on the needles; new droplets are seen growing in Figure S2 (panels d and e). This cycling process (nucleation–growth–roll off) is repeated numerous times throughout the condensation experiment with no evidence of water wetting the superhydrophobic surface. The CA between droplets and the SH surface was maintained above 165° throughout, as shown in Figures 4b, 5, and 6. This is true for both the large droplets pinned by the needles, as well as smaller droplets that randomly nucleate on the SH surface. Condensation experiments have been studied for more than 5 days (see Figure S5) without any indication of water wetting the SH surface or a reduction in contact angle (see Figure S5b and Movie 3).

3.3. Effect of Surface Chemistry and Morphology on Condensation Rates. To determine the relative effectiveness of the hybrid superhydrophobic surface on water collection, condensation experiments were performed on a series of surfaces with different surface chemistries and textures. Flat, smooth surfaces of copper, polyethylene, and silicon (treated with dichlorodimethylsilane) were used to compare flat surfaces that are hydrophilic, hydrophobic with high CA hysteresis (CAH = 25°), and hydrophobic with low CA hysteresis (CAH = < 1°), respectively. Images of the condensation process for these three materials, as well as superhydrophobic polyethylene (SH-PE) and the hybrid surface are shown in Figure 7; water

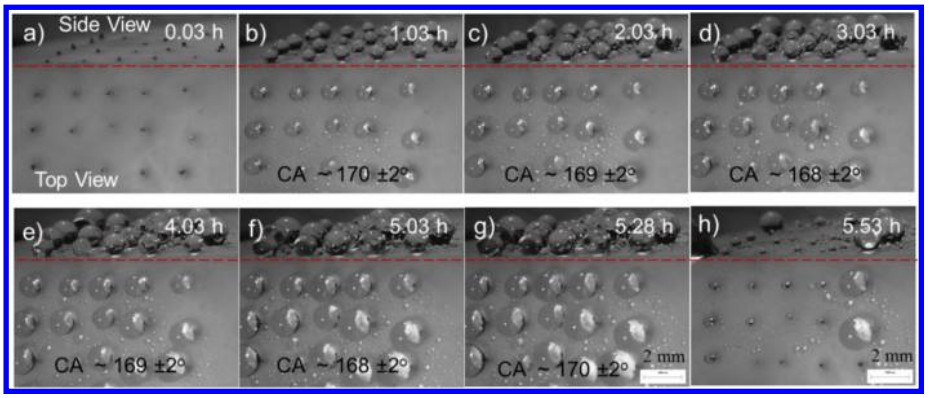

Figure 6. View of the condensation surface recorded every hour during the first cycle of nucleation, growth, and roll-off. Optical microscope images from the top (below red line) and side (above red line) were recorded simultaneously using a 45° mirror: (a) at the beginning of condensation experiment, (b–f) after 1, 2, 3, 4, and 5 h of growth, (g) immediately before roll-off, and (h) after almost all droplets rolled-off the surface (RH, 68 ± 2%; cooling stage temp, 5 °C ; surface temp, 10–12 °C; surface tilt angle, 22°).

DOI: 10.1021/acsami.5b06759
ACS Appl. Mater. Interfaces XXXX, XXX, XXX–XXX

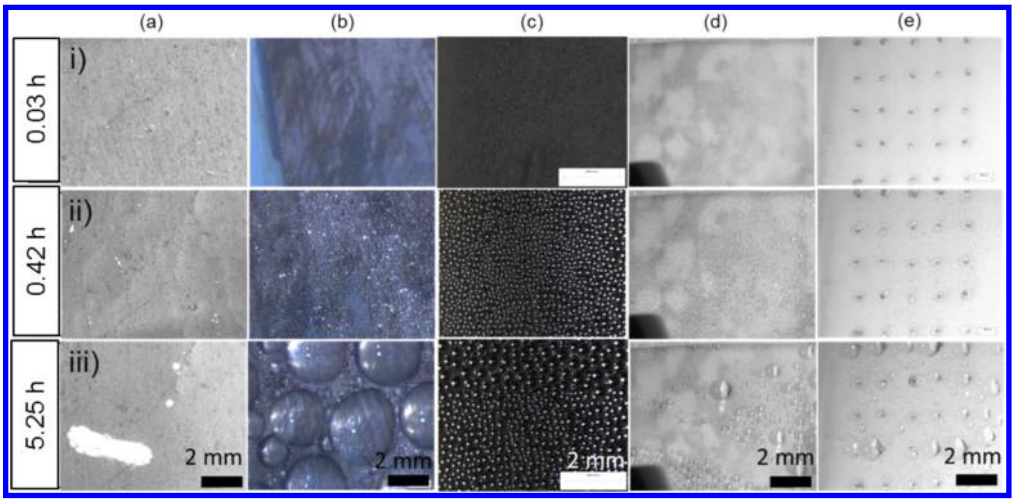

Figure 7. Optical microscope images of condensation of water vapor on surfaces with different wettability and roughness at three stages of the condensation process (0.03, 0.42, and 5.25 h): (a) clean copper, (b) polyethylene film, (c) hydrophobic silicon, and (d) superhydrophobic PE (SH-PE) surface for comparison with a (e) hybrid surface. On most surfaces, initial dropwise condensation leads to the formation of larger droplets. On clean copper, a continuous water film forms after a few minutes (RH, 68 ± 2%; cooling stage temp, 5 °C ; surface temp, 10−12 °C; and surface tilt angle, 33°).

Table 1. Effect of Surface Chemistry and Structure on Condensation Water Collection

substrate	contact angle (degree)	contact angle hysteresis (degree)	time to first roll-off (h)	critical droplet mass (g) $\times 10^{-3}$	water collection rate[a] (mg/mm^2 min) $\times 10^{-3}$
clean copper	<5	> 90	>5	–	0.8 ± 0.1
polyethylene	94	25	>5	14	1.3 ± 0.1
flat hydrophobic silicon	104	3	2	0.2	1.7 ± 0.1
superhydrophobic PE	168	<2	1	0.1	1.6 ± 0.2
hybrid	168	<2[b]	2.5	2.4	3.4 ± 0.1

[a]Average water collection rate and its standard deviation were calculated from three experiments of each surface (RH, 68 ± 2%; cooling stage temp, 5 °C; surface temp, 10−12 °C; and surface tilt angle, 33°). [b]CAH measured on SH background surface.

accumulation rates are compared in Table 1. On the copper surface, filmwise condensation of water occurred exclusively with no droplet formation observed. After only 2 or 3 min, a continuous film of water formed on the surface as shown in Figure 7 (panels a−i). As condensation progressed, the water film became thicker, especially in the downslope region where the leading edge of the water was pinned at the front edge of the copper block (Figure 7 (panels a-ii and iii) and Movie 4). The average water collection rate observed on this surface was the lowest of all surfaces tested 0.8 × 10^{-3} mg/mm^2 min (see Table 1), even though copper has the highest thermal conductivity of any substrate tested. This is due, primarily, to the filmwise condensation process observed on this surface as well as the pinning of water on the edge of the substrate.

On a hydrophobic polyethylene surface, dropwise condensation was observed to occur. Nucleation of droplets occurred uniformly across the surface within 3 min after the beginning of the experiment. Hemispherical drops, consistent with the 94° static CA of water on polyethylene, were clearly visible after 15 min and uniformly covered the surface (Figure 7b-ii and Movie 5). Over time, these droplets continued to grow with adjacent drops merging upon contact to form larger droplets. After 5.25 h, droplet diameters ranged from 3.6 to 4.0 mm. Due to the low receding contact angle of water on this surface (θ_R = 69°) relatively massive droplets (~14 mg or 3.8 mm diameter, see Table 1) were required before roll-off could occur, requiring more than 5 h of condensation time to accumulate. The average condensation rate, measured over the 14−16 h of the experiments was 1.3 × 10^{-3} mg/mm^2 min, which is 63% greater than the rate observed on the copper surface.

By using a hydrophobic Si surface with a low CAH, the critical droplet size required for droplet roll-off was considerably reduced by a factor of 70 from 14 to 0.2 mg. The silanized crystalline silicon surface, with a receding CA (θ_R) of 102° and CAH of 3°, exhibited a high density of nucleated droplets, similar to the polyethylene surface, during the initial stages of the experiment (see Figure 7c and Movie 6). The critical droplet size required for roll-off was smaller; droplets with a mass of 0.2 mg or 0.710 ± 0.016 mm diameter were able to roll off the surface. This roll off process was evident after 2 h, well before the hydrophobic PE[51,57] or hydrophilic clean copper surface. As a consequence, the water collection rate, as measured by the water collection method was increased by 27% compared to untreated PE.

Condensation on the SH-PE surface was similar to the silanized silicon surface (Figure 7d and Movie 7). Drops on both surfaces are highly mobile with CAH in the range of 2−3° and nucleation was observed to occur rapidly upon introduction of moisture. Although the time to the first roll-off event was 50% shorter, and the critical droplet mass was 50% smaller, the overall collection rate was slightly slower (1.6 × 10^{-3} vs 1.7 × 10^{-3} mg/mm^2 min). The slower collection rate may be due to lower thermal conductivity of SH-PE, compared to silicon.

DOI: 10.1021/acsami.5b06759
ACS Appl. Mater. Interfaces XXXX, XXX, XXX−XXX

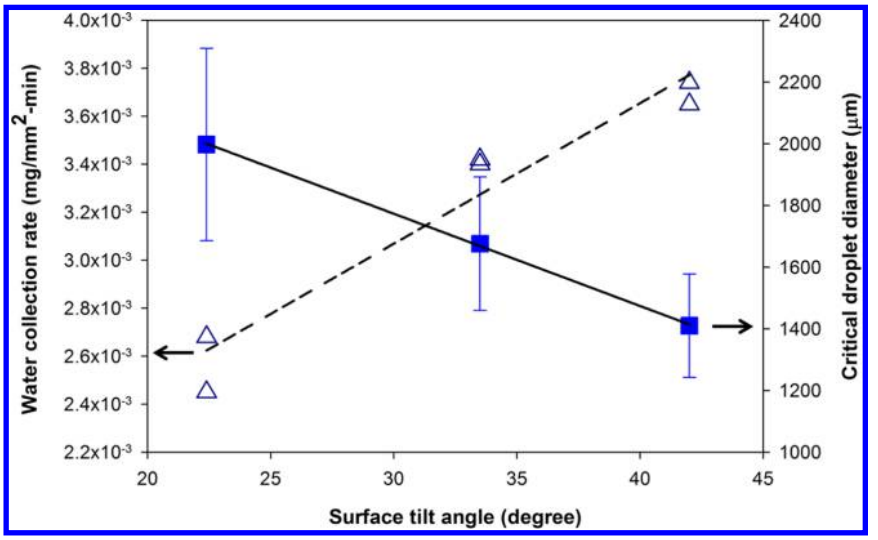

Figure 8. Effect of surface tilt angle on water collection rate and critical droplet diameter at roll-off from the hybrid surface (a hybrid surface with a 5 × 5 needle array at 2 mm pitch, needle height above the surface, 300 μm; RH, 68 ± 2%; needle temperature, 10 °C; surface temperature, 12 °C; and surface tilt angle 33°).

The hybrid surface showed the fastest water collection rate of all samples tested (3.4 × 10^{-3} mg/mm^2 min). This rate is twice as fast as the silanized silicon (flat hydrophobic) surface. Enhanced nucleation and heat transfer on the high aspect-ratio hydrophilic steel needles, as well as the low CAH of the SH-PE surface, combine to enable the higher rate. Moreover, the larger critical droplet mass (2.4 or 0.2 × 10^{-3} g) at similar time to roll-off means that a large swath of the down slope droplets will be imbibed and carried away.

3.4. Effect of Surface Tilt Angle on Water Collection Rate. To study the effect of tilt angle on the water collection rate, the entire condensation chamber was mounted at specific angles relative to the horizontal during the 10−14 h duration experiments. Increasing the tilt angle resulted in an approximately linear increase in the water collection rate as shown in Figure 8. The rate when the surface was tilted at 43° was 50% greater than when tilted at 22°. Dropwise condensation, without wetting of the SH surface, was observed at all tilt angles.

At higher tilt angles, the gravitational force acting on the droplet is greater. As a result, the critical droplet diameter at roll-off decreases from 2.0 to 1.3 mm with tilt angle increasing from 22 to 43° (Figure 8). At least 16 droplet roll-off events were evaluated to calculate the average critical diameter. Reducing the maximum size of the droplets from 2.0 to 1.3 is consistent with higher condensation rates. With decreasing droplet size, the thermal resistance between the outer drop surface (where condensation is occurring) and the needle surface would decrease.

3.5. Effect of Needle Array Pitch on Water Collection Rate. The effect of needle pitch on water collection rates for surfaces with 5 × 5 arrays of needles that are 300 μm above the surface of the SH-PE is shown in Figure 9. As the separation between adjacent needles is increased from 1.0 to 1.5 mm, a 30% increase in water collection rate was observed. This rate remains relatively constant on expanding the pitch to 2.0 mm but decreases by more than 40% when the pitch is further increased to 3.0 mm.

As with the study of needle height, the effect of needle pitch on water collection rates is a balance between competing factors. In this case, the tilt angle (and thus thermal resistance between droplet and needle) is the same for all samples. By placing the needles closer together, droplets coalesce before roll-off, thereby becoming pinned by two needles rather than one. Because the TCL is doubled, a higher critical mass is required before roll-off can occur, depressing the water collection rate. When needles are spaced further apart, coalescence before roll-off does not occur, and high rates are observed. Further increasing the distance to 3.0 mm, suppresses the water collection rate as a larger percentage of the surface is no longer swept by droplets rolling off the surface. In this way, a portion of the surface becomes inactive toward water collection. Interestingly, the optimized needle pitch observed, 1.5 mm, corresponds closely to the pitch of hydrophilic features observed on the Namib beetle elytra;[51] hydrophilic regions more closely or less densely spaced are less efficient at condensing water.

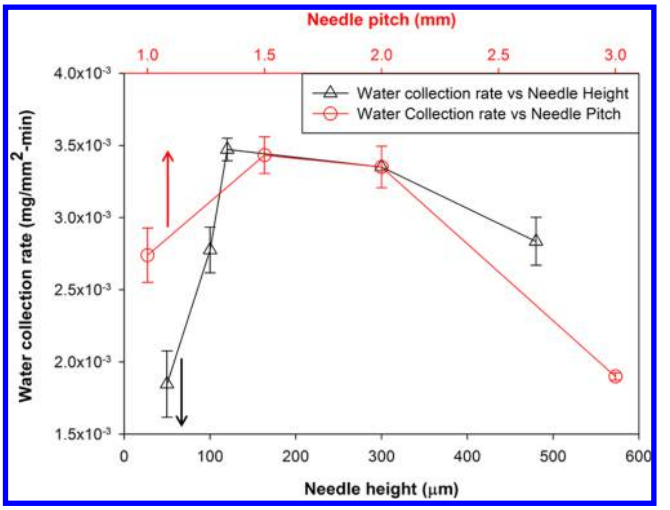

Figure 9. Effect of needle pitch and needle height above the background surface on water collection rate on a hybrid surface (RH, 68 ± 2%; surface temperature, 10−12 °C; surface tilt angle, 33°).

3.6. Effect of Needle Height on the Rate of Condensation. The height of the needles above the superhydrophobic surface affects the water collection rates as

DOI: 10.1021/acsami.5b06759
ACS Appl. Mater. Interfaces XXXX, XXX, XXX−XXX

Table 2. Condensation Experiment Parameters, Measurements, and Calculations

sink set point (°C)	needle tip temp T_{tip} (°C)	vapor temp T_{vap} (°C)	dew point T_{Dew} (°C)	$\Delta T = (T_{dew} - T_{tip})$ (°C)	water collection rate[a] (mg/mm^2 min) $\times 10^{-3}$
1	10.2 ± 1.3	23.4 ± 0.3	16.6 ± 0.3	6.4 ± 1.3	3.31 ± 0.02
5	12.5 ± 0.7	23.8 ± 0.5	17.8 ± 0.8	5.3 ± 1.1	3.35 ± 0.14
9	15.2 ± 0.4	24.2 ± 0.6	19.0 ± 0.4	3.8 ± 0.7	2.42 ± 0.04

[a]Water collection rate is the average of three experiments based on the total water collected over the 10−14 h (needle height, 300 μm; needle array pitch, 2 mm; % RH, 70 ± 2; and surface tilt angle, 33°).

shown in Figure 9 with a hybrid surface composed of a 5 × 5 needle array at 2 mm pitch. As the height above the surface increases from 50 to 120 μm, a rapid increase in water collection rate from 1.8 × 10^{-3} to 3.5 × 10^{-3} mg/mm^2 min is observed. When the needles extend a relatively short distance, the area for heat transfer between the droplet and the needle is limited. Thus, the water collection rate for needles extending 50 μm above the surface is the lowest observed and only 30% greater than for a superhydrophobic surface without any needles (Figure 9). As the needle height is increased, the water collection rate increases, reaching a maximum rate at a height of 120 μm. The rate remains relatively constant, decreasing only slightly at a height of 300 μm. Above this value, the water collection rate decreases such that at a height of 480 μm the rate is reduced by 18% from the maximum.

There are several competing factors that explain these trends. As the height increases, heat transfer between the drop and the needle increases owing to the larger contact surface area. This explains the initial, sharp increase in water collection rates. However, as the needle length increases, so does the TCL, thus increasing the force pinning the droplet to the needle surface. With increasing droplet size, heat transfer between the outer drop surface (where condensation is occurring) and the needle would be expected to decrease due to the increased distance over which the heat would need to be conducted. Significant convection within the droplet would be required to mitigate this increased distance. On the basis of the data, the balance of improved heat transfer resulting from the larger needle is not sufficient to overcome the larger critical droplet mass to achieve roll-off. Thus, the water collection rate shows a gradual decline at needle heights above 120 μm.

3.7. Effect of Cooling Stage Temperature on Water Collection. Reducing the temperature of the steel needles generally results in faster condensation rates as the heat can be conducted away from the needle tips more rapidly. The needle tip temperature is controlled indirectly by adjusting the fluid temperature that flows through the sink to which the needles are thermally coupled. However, the cooler environment within the chamber can also affect the dew point (i.e., the temperature at which air becomes saturated with water vapor) of the vapor above the needles. For a given needle tip temperature, a higher dew point would result in a more rapid condensation rate. Thus, it is the difference between dew point and needle temperature (ΔT) that correlates with condensation rate.[58] Temperatures within the condensation chamber for three different conditions are shown in Table 2. Increasing the ΔT from 3.8 to 6.4 °C results in a 38% increase in water condensation rate from 24.2 × 10^{-4} to 33.5 × 10^{-4}mg/mm^2 min. This higher rate is due, primarily, to the lower tip temperature. Further reduction in the tip temperature, however, did not lead to an increased condensation rate because the dew point temperature also decreased, resulting in no net change in ΔT. Uncertainties in the tip temperature and dew point may partially obscure the trends.

3.8. Heat Transfer Study. *3.8.1. Bulk Temperature Measurements.* Figure 10 presents the variation in needle temperature over a 24 h period, where T1 is the thermistor closest to the needle tip, T2 is the middle thermistor, and T3 is the thermistor at the base of the needle (Figure 3). Each test consisted of three sections: room temperature with dry air, 5 °C set point with dry air, and 5 °C set point with humid air (see the Experimental section for details).

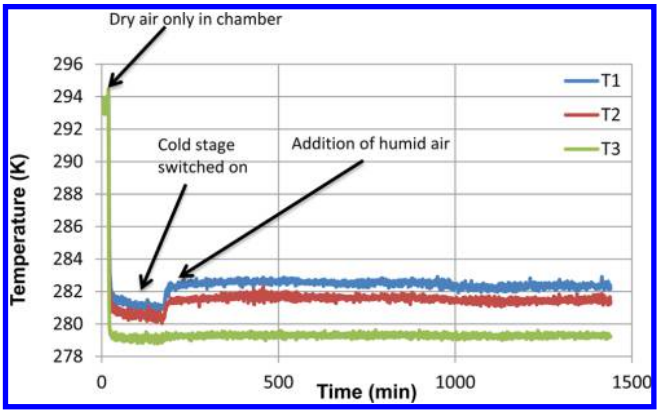

Figure 10. Sample temperature versus time plot showing the temperature profile of the needle for a test lasting 24 h in duration.

3.8.2. Heat Dissipation. The formation of condensate on the needle tip is the result of cooling a saturated vapor below its saturation limit. At this point, the vapor changes from a gas phase to a liquid phase. This change in phase results in a release of heat to the surrounding environment. The hydrophilic needles act as both nucleation sites for the formation of condensation and as heat sinks absorbing a quantity of the heat being dissipated during the condensation process.

The addition of saturated vapor resulted in a step increase of 1.5 K in the temperatures measured by the two thermistors, T1 and T2, closest to the needle tip. This rise in temperature can be attributed to the formation of condensate drops on the needle. During the change of phase from vapor to liquid, a significant quantity of energy is released which is then conducted along the needle. After this initial temperature rise, however, there are no further step increases in temperature and an almost steady state condition is reached.

Figure S6 is a plot of the heat dissipated into the needle during the condensation process as calculated using eq 1. The data points were interpreted from the recorded temperature data at 20 min intervals. Figure S6 shows that after the initial increase in heat dissipation, from 0.33 mJ/s to approximately 0.58 mJ/s, a relatively constant rate of heat dissipation is seen, which results in an average heat dissipation of ~0.55 mJ/s with a standard deviation of 0.043 mJ/s. During the condensation

DOI: 10.1021/acsami.5b06759
ACS Appl. Mater. Interfaces XXXX, XXX, XXX−XXX

process, a high level of heat dissipation is indicative of a high condensation rate. By the same logic, a steady rate of heat dissipation indicates a steady condensation rate. The results show that approximately 100 min after the addition of the saturated air to the condensation chamber, an almost constant rate of heat dissipation is seen, indicating that a relatively constant condensation rate should exist on the needle tip.

3.8.3. Heat Transfer Coefficient. Conventional condenser surfaces are made of metals and exhibit filmwise condensation rather than dropwise condensation. The latter, however, is more desirable as droplets can be efficiently removed from the surface in order to significantly enhance the heat transfer performance; typically heat transfer coefficients for dropwise condensation can be up to an order of magnitude larger than those seen in filmwise condensation.[58,59] The effective heat transfer coefficient of the needle tip was extracted from the temperature data by examining the energy balance that exists between the needle and the surrounding environment. It is assumed that a convection-conduction balance exists at the needle tip. The energy that is released during the condensation process is convected from the condensate to the needle tip from which the energy is then conducted through the needle. This assumption was validated in two ways: the first involved calculating the characteristic Rayleigh number for a condensate droplet and the second involved the development of an analytical model of the problem. The Rayleigh number, $Ra_D = g\beta\Delta TD^3/\nu\alpha$ (where g = gravity, β = thermal expansion coefficient, ΔT = temperature change, D = diameter, ν = kinematic viscosity, and α = thermal diffusivity), is a dimensionless number that expresses the ratio of buoyancy forces to viscous forces, modulated by the Prandtl number. In buoyancy driven flow, it can be used to determine whether the heat transfer in a fluid is primarily driven by convection or conduction. When the Rayleigh number is less than 1 ($Ra < 1$), heat transfer is primarily conductive; when Ra exceeds this critical value, convective heat transfer begins to dominate. Early in the experiment, the condensate drop diameter is small (~100 μm), with a $\Delta T = 5$, where ΔT is the temperature difference between the dew point and the needle tip, the characteristic Rayleigh number is ~1.1. Hence, convection is the primary mode of heat transfer within the droplet. Over time, as the condensation process continues and the droplet increases in diameter, the Ra increases to Ra ~ 200 at D = 500 μm and to $Ra > 1000$ at D = 1000 μm. Thus, over time, convection becomes the dominant mode of heat transfer within the condensate drops. .

The second validation method involved the development of a transient model of the problem, where the transient conduction in eq 3 is solved using a finite difference technique.

$$\frac{\delta^2 T}{\delta x^2} = \frac{1}{\alpha}\frac{\delta T}{\delta x} \tag{3}$$

The solution is subject to the following assumptions: (1) it is assumed that both the needle and the condensate have constant properties. (2) There is no internal heat generation within the needle. (3) The temperature is uniform across the needle cross section. (4) That heat is only conducted along the length of the needle.

Other critical components of the model are the boundary and initial conditions applied to the needle. At the base, the needle was subject to a constant temperature boundary condition. While at the tip a convection−conduction energy balance boundary condition was applied, which was validated with the characteristic Rayleigh number of the condensate drops. A temperature gradient was imposed along the length of the needle as an initial condition. A detailed description of the model can be found in section 2 of the Supporting Information.

Figure S7 presents the change in effective heat transfer coefficient of the needle over time. Measurements were calculated at 20 min intervals from t = 0 min to t = 1245 min. Similar to Figure 10, the heat transfer coefficient experiences a sharp increase at t = 0 min from 135 W/m^2 K, when the saturated vapor enters the condensation chamber, to ~240 W/m^2 K. After this initial increase, however, the effective heat transfer coefficient remains relatively constant and has an average value of ~220 W/m^2 K with a standard deviation of 17.9 W/m^2 K over the time period from 100 to 1240 min.

The value of 220 W/m^2 K is the effective heat transfer coefficient between the condensate and a single needle in the array. Scaling this value up for the entire 25 needle array results in an effective heat transfer coefficient of 5500 W/m^2 K. Yun et al.[60] report heat transfer coefficients for filmwise condensation on a stainless steel surface of approximately 1500 W/m^2 K. The value reported in the present study, 5500 W/m^2 K, is 3.7 times greater than the filmwise case. A table comparing rates of heat dissipation and heat transfer coefficients of different surfaces which promote dropwise and/or filmwise condensation is given in Table S2.

The previously described image analysis of the surface, Section 3.2 provided details of condensate drop growth rates also revealed a number of events, such as droplet roll-offs and droplet coalescence, occurring on the hybrid superhydrophobic surface. These events were not detected by the thermal instrumentation. This was not, however, due to a lack of sensitivity in the instrumentation. The previously described analytical model was also used to determine the thermal time constant of the needle. This value is the time required by the needle to reach 63.2% of its final value after a step change in temperature at the needle tip. The thermal time constant of the needle was found to be 2.53 s, while the thermistors have a response time of 30 ms, indicating that the instrumentation was more than adequate to detect these droplet events on the needle tip. The lack of events seen in the temperature data is due to the hydrophilicity of the needles. The needles that protrude through the superhydrophobic surface are hydrophilic, and once a droplet rolls off, a thin layer of water remains and coats the needle surface. Due to the presence of this film, the thermal step change after a condensate drop rolls off the needle is not sufficiently large to be detected by the instrumentation.

3.8.4. Inferred Condensation Rate. Both the heat dissipation rates and effective heat transfer coefficient data provide some novel insights into the thermal behavior exhibited during the formation of a condensate drop on the needle. Ultimately, it is the condensation rate of the surface that is of primary interest. The overall condensation rate on the needle ($\dot{m}$) was calculated using eq 4, presented previously by Incropera.[58]

$$\dot{m} = \frac{h_{\text{eff}} A_{\text{exp}} (T_{\text{dew}} - T_{\text{tip}})}{h_{fg}} \tag{4}$$

where h_{eff} is the effective heat transfer coefficient, A_{exp} is the surface area of the needle tip that is exposed to the saturated vapor, T_{dew} is the dew point temperature, T_{tip} is the inferred needle tip temperature, and h_{fg} is the specific enthalpy of the saturated vapor.

DOI: 10.1021/acsami.5b06759
ACS Appl. Mater. Interfaces XXXX, XXX, XXX−XXX

Figure 11 is a plot of the change in inferred condensation rate of the needle with time. Similar to Figures S6 and S7 after

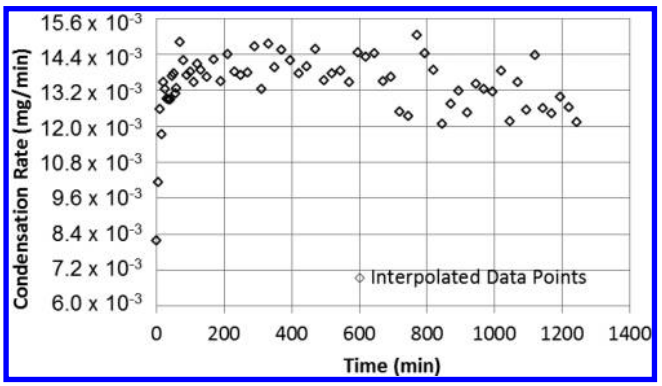

Figure 11. Plot of condensation rate on needle with time.

the addition of the saturated vapor to the condensation chamber, a rapid increase in condensation on the needle occurs, from ~8.4 × 10^{-3} to 14.4 × 10^{-3} mg/min. Subsequently, the condensation rate on the needle stabilizes and reaches an average condensation rate of 13.2 × 10^{-3} mg/min, with a standard deviation of 1.7 × 10^{-3} mg/min from 100 to 1240 min. As it was stated previously in Section 3.2, that if a steady rate of heat was being dissipated into the needle then a constant rate of condensation was occurring on the needle, the data in Figure 11 validates this argument. The relatively constant condensation rate, ~13.2 × 10^{-3} mg/min, can be attributed to two things: the previously described wettability of the needle and the conditions within the chamber. After a period of approximately 100 min, the humidity levels in the chamber have reached a constant level. The constant surface condition of the needle, due to the presence of the liquid film, and the constant humidity level in the condensation chamber result in an almost constant condensation rate on the needle.

3.8.5. Comparison of Rate of Condensation from Water Collection and Heat Transfer Study. The condensation rate calculated from the heat transfer study is in good agreement with condensation rates determined using the two different experimental methods as summarized in Table 3. In the heat transfer study, the condensation rate was calculated to be 13.2 × 10^{-3} (±1.7× 10^{-3}) mg/min based on data from only the needle labeled no. 1 in Figure S8. The condensation rate on this same needle was also determined experimentally by measuring the diameter of droplets immediately before roll-off and summing the calculated volumes over the duration of the experiment. In this case, the condensation rate was the same as that determined from the heat transfer study: 13.2 × 10^{-3} mg/min.

The overall water collection rate for this hybrid surface consisting of a 5 × 5 needle array (needle height = 300 μm, needle pitch = 2 mm, tilt angle = 33°, and cooling stage temperature = 5 °C) was measured to be 261.9 × 10^{-3} mg/min as determined by weighing the total water collected. Assuming uniform behavior for each needle, the collection rate per needle would be 10.5 × 10^{-3} mg/min. This average value is 20% lower than the value for needle no. 1 (see above and Table 3). The drop diameter method can be used to calculate an average collection rate as well. With the use of data from seven of the 25 needles in the array (labeled in Figure S8), an average value for the water collection rate was calculated to be 285.0 × 10^{-3} mg/min in good agreement (~8% difference) with the water weighing method. This result indicates that the condensation rate on all needles is not the same and that needle no. 1 experiences an accumulation rate higher than average.

Considering the position of needle no. 1 within the condensation chamber, a higher rate of condensation is not surprising. Needle no. 1 was located closer to the vapor inlet port than the other needles in the array. Thus, the higher local RH would result in higher condensation rates. The overall good agreement between condensation rates determined from various measurement techniques supports the heat transfer model presented in Sections 3.8.3 and 3.8.4.

Additional support for the thermal model was obtained by measuring the water condensation rate as a function of needle thermal conductivity. If the rate limiting step for condensation was conduction of heat along the needle (5.4 mm in length) then increasing the thermal conductivity of the needle would increase the condensation rate. To test this hypothesis, a hybrid surface was fabricated using tungsten (k = 173 W m^{-1} K^{-1}) rather than steel (k = 50 W m^{-1} K^{-1}) needles. The water collection rates for these two needle materials, however, were the same within experimental error (3.6 × 10^{-3} ± 0.4 × 10^{-3} mg/mm^2 min vs 3.4 × 10^{-3} ± 0.1 × 10^{-3} mg/mm^2 min for tungsten and steel, respectively).

From this result, we can conclude that the rate-limiting step for water condensation is thermal transport from the vapor−liquid interface, across the droplet to the needle. This is consistent with the model presented in section 3.8.3 and the high Rayleigh number within the growing droplet. The relatively high thermal resistance across the droplet is consistent with the effect of experimental variables on condensation rates. For example, increasing the tilt angle increases the condensation rate because the critical droplet diameter (and thus the thermal resistance) is smaller. Similarly, increasing the needle height will reduce the distance (and thus the thermal resistance) between the droplet surface and the needle.

Table 3. Condensation Rates from Heat Transfer Study, Roll-off Water Droplet Diameter Measurement, And Water Collection Study

	Condensation rate (mg/min)			
		determined from measurement of droplet diameter before roll-off		
	calculated from effective heat transfer coefficient	using needle #1 only	using average of 7 needles	determined using total mass of water collected
condensation rate per needle	13.2 × 10^{-3}	13.2 × 10^{-3}	11.4 × 10^{-3}	10.5 × 10^{-3}
condensation rate for full array of 25 needles	330.0 × 10^{-3}	330.0 × 10^{-3}	285.0 × 10^{-3}	261.9 × 10^{-3}

DOI: 10.1021/acsami.5b06759
ACS Appl. Mater. Interfaces XXXX, XXX, XXX−XXX

4. CONCLUSION

A hybrid superhydrophobic−hydrophilic surface was fabricated by impaling a superhydrophobic polymer film onto an array of steel needles thermally connected to a heat sink. Due to the greater wettability and lower temperature (ΔT = 2 °C) of the metal surface, water vapor preferentially nucleates and grows on the needle tips. As condensation continues and droplets pinned on the needles grow, the droplets remain in the superhydrophobic Cassie state; no transition to a wetted (i.e., Wenzel) state was observed even after more than 5 days of continuous operation. When the droplets reach a critical mass, gravitational forces overcome the forces at the triple contact line freeing the droplet, which separates from the needle and rolls off the tilted substrate. As the droplet rolls-off, it collides with and imbibes small droplets condensed on the superhydrophobic surface as well as other, smaller, drops pinned on downslope needles. This leaves the needles and a swath of SH surface clear of liquid water and ready for another cycle of nucleation and droplet growth.

Condensation rates on the hybrid superhydrophobic−hydrophilic surface were twice as fast as either a superhydrophobic surface alone or a silane-treated silicon surface with CA 104° and CAH of 3° and 4 times greater than pure copper. This demonstrates the improvement that a combination of dropwise condensation and selective nucleation can have on heat transfer efficiency.

The geometry of the hybrid surface was shown to affect condensation rates. Maxima were observed for both needle height and needle pitch, illustrating trade-offs between effective heat-transfer and droplet pinning on the hydrophilic needle surface. Water collection rates increase with higher tilt angles as smaller droplets can roll-off the surface and roll-off events occur more frequently. The optimal condensation performance was obtained with a 5 × 5 needle array on 1.5 mm pitch, raised 120 μm above the surface and tilted at an angle of 43°. These dimensions are similar in size and scale to those of the Namib beetle elytra.[51]

A model of the heat transport was developed based on the assumption that a convection−conduction balance exists at the needle tip. Energy released during the condensation process is convected from the vapor−liquid interface to the needle tip from which the energy is then conducted through the needle. This model is consistent with the high R_a for the droplet as well as the excellent agreement between experimental and calculated water collection rates. Increasing the thermal conductivity of the needle does not affect water collection rates, indicating the importance of convection within the droplet to transport heat and increase water condensation rates.

The combination of high condensation rates with the availability of large area, low-cost, robust, superhydrophobic polymer substrates makes hybrid superhydrophobic−hydrophilic surfaces a viable approach for the construction of efficient heat transfer and water collection devices.

■ ASSOCIATED CONTENT

Supporting Information

The Supporting Information is available free of charge on the ACS Publications website at DOI: 10.1021/acsami.5b06759.

Images of water collection assembly, continuous dropwise condensation, thermistor positioning along a needle, SEM images of SH surface, condensation surface after 5.5 days of continuous operation, a plot of effective heat transfer coefficient of the needle tip over time and surface with needles numbered and flow direction indicated, and calculations of nucleation rate and details of the heat transfer measurement model (PDF)

Water condensation on the hybrid superhydrophobic−hydrophilic surface (AVI)

Water condensation process (in a side view close up) on the hybrid superhydrophobic−hydrophilic surface (AVI)

Water vapor condensation for ∼5.5 days on a hybrid superhydrophobic−hydrophilic surface (AVI)

Condensation on a clean copper substrate (AVI)

Water condensation on a hydrophobic polyethylene film substrate (AVI)

Water condensation on a hydrophobic silicon surface made by chemical vapor deposition (CVD) of dimethylydicholorsilane (DMDCS) on a clean silicon surface (AVI)

Water condensation on a superhydrophobic surface directly placed on the cooling stage (AVI)

■ AUTHOR INFORMATION

Corresponding Author

*E-mail: Alan.Lyons@csi.cuny.edu.

Notes

The authors declare the following competing financial interest(s): Alan Lyons is co-founder and CTO of ARL Designs LLC.

■ ACKNOWLEDGMENTS

B.M. and A.M.L. acknowledge support from the NYS Empire State Development's Division of Science, Technology & Innovation (NYSTAR) and the CUNY Center for Advanced Technology. Q.F.X. and A.M.L. acknowledge support from the National Science Foundation SBIR Phase II program (Scratch and Abrasion Resistant Superhydrophobic Polymer Coatings, Contract: 1330949). M.M.G.E., V.E., and J.P. acknowledge the financial support of Science Foundation Ireland under Grant 10/CE/11853 and gratefully acknowledge the financial support of the Irish Research Council through the Embark Initiative. We would like to thank Marc Hodes (Tufts University) for helpful discussions and aerogel samples and Paul Kolodner for the thermistors. The laboratory assistance of Mark Barahman, Thomas Huang, Queenie Li, and Yong He (Dan) Liu is greatly appreciated.

■ REFERENCES

(1) Carey, V. P. *Liquid-Vapor Phase-Change Phenomena: An Introduction to the Thermophysics of Vaporization and Condensation Processes in Heat Transfer Equipment*; Taylor and Francis: New York, 2007.

(2) Rose, J. W. Dropwise Condensation Theory and Experiment: a Review. *Proc. Inst. Mech. Eng., Part A* **2002**, *216*, 115−128.

(3) Patankar, N. A. Supernucleating Surfaces for Nucleate Boiling and Dropwise Condensation Heat Transfer. *Soft Matter* **2010**, *6*, 1613−1620.

(4) Bhardwaj, R.; ten Kortenaar, M. V.; Mudde, R. F. Influence of Condensation Surface on Solar Distillation. *Desalination* **2013**, *326*, 37−45.

(5) Lara, J. R.; Holtzapple, M. T. Experimental Investigation of Dropwise Condensation on Hydrophobic Heat Exchangers. Part II: Effect of Coatings and Surface Geometry. *Desalination* **2011**, *280*, 363−369.

DOI: 10.1021/acsami.5b06759
ACS Appl. Mater. Interfaces XXXX, XXX, XXX−XXX

(6) Lara, J. R.; Holtzapple, M. T. Experimental Investigation of Dropwise Condensation on Hydrophobic Heat Exchangers. Part I: Dimpled-Sheets. *Desalination* **2011**, *278*, 165−172.
(7) Garrod, R. P.; Harris, L. G.; Schofield, W. C. E.; McGettrick, J.; Ward, L. J.; Teare, D. O. H.; Badyal, J. P. S. Mimicking a Stenocara Beetle's Back for Microcondensation Using Plasmachemical Patterned Superhydrophobic−Superhydrophilic Surfaces. *Langmuir* **2007**, *23*, 689−693.
(8) Zhang, X. T.; Jin, M.; Liu, Z. Y.; Tryk, D. A.; Nishimoto, S.; Murakami, T.; Fujishima, A. Superhydrophobic TiO2 Surfaces: Preparation, Photocatalytic Wettability Conversion, and Superhydrophobic-Superhydrophilic Patterning. *J. Phys. Chem. C* **2007**, *111*, 14521−14529.
(9) Thickett, S. C.; Neto, C.; Harris, A. T. Biomimetic Surface Coatings for Atmospheric Water Capture Prepared by Dewetting of Polymer Films. *Adv. Mater.* **2011**, *23*, 3718−3722.
(10) Ke, Q. P.; Zhang, S. A.; Tang, T. D.; Wang, S.; Jing, H. L. Intrinsic Dew-Enhancing Ability of SiO_2/PODS Materials. *Colloids Surf., A* **2011**, *377*, 110−114.
(11) Miljkovic, N.; Enright, R.; Nam, Y.; Lopez, K.; Dou, N.; Sack, J.; Wang, E. N. Jumping-Droplet-Enhanced Condensation on Scalable Superhydrophobic Nanostructured Surfaces. *Nano Lett.* **2013**, *13*, 179−187.
(12) Das, A.; Kilty, H.; Marto, P.; Andeen, G.; Kumar, A. The Use of an Organic Self-Assembled Monolayer Coating to Promote Dropwise Condensation of Steam on Horizontal Tubes. *J. Heat Transfer* **2000**, *122*, 278−286.
(13) Depew, C. A.; Reisbig, R. L. Vapor Condensation on a Horizontal Tube Using Teflon to Promote Dropwise Condensation. *Ind. Eng. Chem. Process Des. Dev.* **1964**, *3*, 365−369.
(14) Erb, R.; Thelen, E. Promoting Permanent Dropwise Condensation. *Ind. Eng. Chem.* **1965**, *57*, 49−52.
(15) Rose, J. W.; Glicksman, L. R. Dropwise Condensation-The Distribution of Drop Sizes. *Int. J. Heat Mass Transfer* **1973**, *16*, 411−425.
(16) Glicksman, L. R.; Hunt, A. W., Jr Numerical Simulation of Dropwise Condensation. *Int. J. Heat Mass Transfer* **1972**, *15*, 2251−2269.
(17) Chung, B. J.; Kim, S.; Kim, M. C.; Ahmadinejad, M. Experimental Comparison of Film-Wise and Drop-Wise Condensations of Steam on Vertical Flat Plates with the Presence of Air. *Int. Commun. Heat Mass Transfer* **2004**, *31*, 1067−1074.
(18) Vemuri, S.; Kim, K. J.; Wood, B. D.; Govindaraju, S.; Bell, T. W. Long Term Testing for Dropwise Condensation Using Self-Assembled Monolayer Coatings of N-Octadecyl Mercaptan. *Appl. Therm. Eng.* **2006**, *26*, 421−429.
(19) Gensler, R.; Grassmann, A.; Waidhas, M., (Siemens Corporation, USA). Coating for Vapor Condensers. U.S. Patent 2010/0129645, 2010.
(20) Bonner, R. W. Dropwise Condensation Life Testing of Self Assembled Monolayers. *Proc. ASME Int. Heat Transfer Conf.* **2010**, *2*, 221−226.
(21) Citakoglu, E.; Rose, J. W. Dropwise Condensation-Some Factors Influencing the Validity of Heat-Transfer Measurements. *Int. J. Heat Mass Transfer* **1968**, *11*, 523−537.
(22) Paxson, A. T.; Yagüe, J. L.; Gleason, K. K.; Varanasi, K. K. Stable Dropwise Condensation for Enhancing Heat Transfer via the Initiated Chemical Vapor Deposition (iCVD) of Grafted Polymer Films. *Adv. Mater.* **2014**, *26*, 418−423.
(23) Bansal, G. D.; Khandekar, S.; Muralidhar, K. Measurement of Heat Transfer During Drop-Wise Condensation of Water on Polyethylene. *Nanoscale Microscale Thermophys. Eng.* **2009**, *13*, 184−201.
(24) Miljkovic, N.; Xiao, R.; Preston, D. J.; Enright, R.; McKay, I.; Wang, E. N. Condensation on Hydrophilic, Hydrophobic, Nanostructured Superhydrophobic and Oil-Infused Surfaces. *J. Heat Transfer - Trans. ASME* **2013**, *135*, 080906.
(25) Miljkovic, N.; Enright, R.; Wang, E. N. Effect of Droplet Morphology on Growth Dynamics and Heat Transfer during Condensation on Superhydrophobic Nanostructured Surfaces. *ACS Nano* **2012**, *6*, 1776−1785.
(26) Miljkovic, N.; Preston, D. J.; Enright, R.; Wang, E. N. Electrostatic Charging of Jumping Droplets. *Nat. Commun.* **2013**, *4*, 2517.
(27) Hancock, M. J.; Demirel, M. C. Anisotropic Wetting on Structured Surfaces. *MRS Bull.* **2013**, *38*, 391−396.
(28) Yin, L.; Wang, Y. Y.; Ding, J. F.; Wang, Q. J.; Chen, Q. M. Water Condensation on Superhydrophobic Aluminum Surfaces with Different Low-Surface-Energy Coatings. *Appl. Surf. Sci.* **2012**, *258*, 4063−4068.
(29) Ko, T. J.; Her, E. K.; Shin, B.; Kim, H. Y.; Lee, K. R.; Hong, B. K.; Kim, S. H.; Oh, K. H.; Moon, M. W. Water Condensation Behavior on the Surface of a Network of Superhydrophobic Carbon Fibers with High-Aspect-Ratio Nanostructures. *Carbon* **2012**, *50*, 5085−5092.
(30) Feng, J.; Qin, Z. Q.; Yao, S. H. Factors Affecting the Spontaneous Motion of Condensate Drops on Superhydrophobic Copper Surfaces. *Langmuir* **2012**, *28*, 6067−6075.
(31) Cheng, J. T.; Vandadi, A.; Chen, C. L. Condensation Heat Transfer on Two-Tier Superhydrophobic Surfaces. *Appl. Phys. Lett.* **2012**, *101*, 131909.
(32) Dorrer, C.; Ruhe, J. Condensation and Wetting Transitions on Microstructured Ultrahydrophobic Surfaces. *Langmuir* **2007**, *23*, 3820−3824.
(33) Rykaczewski, K.; Scott, J. H. J.; Rajauria, S.; Chinn, J.; Chinn, A. M.; Jones, W. Three Dimensional Aspects of Droplet Coalescence During Dropwise Condensation on Superhydrophobic Surfaces. *Soft Matter* **2011**, *7*, 8749−8752.
(34) Boreyko, J. B.; Chen, C. H. Self-Propelled Dropwise Condensate on Superhydrophobic Surfaces. *Phys. Rev. Lett.* **2009**, *103*, 184501.
(35) Chen, C. H.; Cai, Q. J.; Tsai, C. L.; Chen, C. L.; Xiong, G. Y.; Yu, Y.; Ren, Z. F. Dropwise Condensation on Superhydrophobic Surfaces with Two-Tier Roughness. *Appl. Phys. Lett.* **2007**, *90*, 173108.
(36) Narhe, R. D.; Beysens, D. A. Water Condensation on a Super-Hydrophobic Spike Surface. *Europhys. Lett.* **2006**, *75*, 98−104.
(37) Wier, K. A.; McCarthy, T. J. Condensation on Ultrahydrophobic Surfaces and Its Effect on Droplet Mobility: Ultrahydrophobic Surfaces are not Always Water Repellant. *Langmuir* **2006**, *22*, 2433−2436.
(38) Rykaczewski, K.; Scott, J. H. J. Methodology for Imaging Nano-to-Microscale Water Condensation Dynamics on Complex Nanostructures. *ACS Nano* **2011**, *5*, 5962−5968.
(39) Rykaczewski, K.; Scott, J. H. J.; Fedorov, A. G. Electron Beam Heating Effects During Environmental Scanning Electron Microscopy Imaging of Water Condensation on Superhydrophobic Surfaces. *Appl. Phys. Lett.* **2011**, *98*, 093106.
(40) Dorrer, C.; Rühe, J. Wetting of Silicon Nanograss: From Superhydrophilic to Superhydrophobic Surfaces. *Adv. Mater.* **2008**, *20*, 159−163.
(41) Narhe, R. D.; Beysens, D. A. Growth Dynamics of Water Drops on a Square-Pattern Rough Hydrophobic Surface. *Langmuir* **2007**, *23*, 6486−6489.
(42) Enright, R.; Miljkovic, N.; Alvarado, J. L.; Kim, K.; Rose, J. W. Dropwise Condensation on Micro-and Nanostructured Surfaces. *Nanoscale Microscale Thermophys. Eng.* **2014**, *18*, 223−250.
(43) Miljkovic, N.; Preston, D. J.; Enright, R.; Wang, E. N. Electric-Field-Enhanced Condensation on Superhydrophobic Nanostructured Surfaces. *ACS Nano* **2013**, *7*, 11043−11054.
(44) Torresin, D.; Tiwari, M. K.; Del Col, D.; Poulikakos, D. Flow Condensation on Copper-Based Nanotextured Superhydrophobic Surfaces. *Langmuir* **2013**, *29*, 840−848.
(45) Anand, S.; Paxson, A. T.; Dhiman, R.; Smith, J. D.; Varanasi, K. K. Enhanced Condensation on Lubricant-Impregnated Nanotextured Surfaces. *ACS Nano* **2012**, *6*, 10122−10129.
(46) Xiao, R.; Miljkovic, N.; Enright, R.; Wang, E. N. Immersion Condensation on Oil-Infused Heterogeneous Surfaces for Enhanced Heat Transfer. *Sci. Rep.* **2013**, *3*, 1988.

DOI: 10.1021/acsami.5b06759
ACS Appl. Mater. Interfaces XXXX, XXX, XXX−XXX

(47) Rykaczewski, K.; Paxson, A. T.; Staymates, M.; Walker, M. L.; Sun, X. D.; Anand, S.; Srinivasan, S.; McKinley, G. H.; Chinn, J.; Scott, J. H. J.; Varanasi, K. K. Dropwise Condensation of Low Surface Tension Fluids on Omniphobic Surfaces. *Sci. Rep.* **2014**, *4*, 4158.
(48) Dorrer, C.; Ruhe, J. Mimicking the Stenocara Beetle-Dewetting of Drops From a Patterned Superhydrophobic Surface. *Langmuir* **2008**, *24*, 6154−6158.
(49) Chatterjee, A.; Derby, M. M.; Peles, Y.; Jensen, M. K. Condensation Heat Transfer on Patterned Surfaces. *Int. J. Heat Mass Transfer* **2013**, *66*, 889−897.
(50) Derby, M. M.; Chatterjee, A.; Peles, Y.; Jensen, M. K. Flow Condensation Heat Transfer Enhancement in a Mini-Channel with Hydrophobic and Hydrophilic Patterns. *Int. J. Heat Mass Transfer* **2014**, *68*, 151−160.
(51) Parker, A. R.; Lawrence, C. R. Water Capture by a Desert Beetle. *Nature* **2001**, *414*, 33−34.
(52) Varanasi, K. K.; Hsu, M.; Bhate, N.; Yang, W. S.; Deng, T. Spatial Control in the Heterogeneous Nucleation of Water. *Appl. Phys. Lett.* **2009**, *95*, 094101.
(53) Hou, Y.; Yu, M.; Chen, X.; Wang, Z.; Yao, S. Recurrent Filmwise and Dropwise Condensation on a Beetle Mimetic Surface. *ACS Nano* **2015**, *9*, 71−81.
(54) Rykaczewski, K. Microdroplet Growth Mechanism During Water Condensation on Superhydrophobic Surfaces. *Langmuir* **2012**, *28*, 7720−7729.
(55) Yamada, Y.; Ikuta, T.; Nishiyama, T.; Takahashi, K.; Takata, Y. Droplet Nucleation on a Well-Defined Hydrophilic−Hydrophobic Surface of 10 nm Order Resolution. *Langmuir* **2014**, *30*, 14532−14537.
(56) Barahman, M.; Lyons, A. M. Ratchetlike Slip Angle Anisotropy on Printed Superhydrophobic Surfaces. *Langmuir* **2011**, *27*, 9902−9909.
(57) Lee, A.; Moon, M. W.; Lim, H.; Kim, W. D.; Kim, H. Y. Water Harvest via Dewing. *Langmuir* **2012**, *28*, 10183−10191.
(58) Incropera, F. P.; DeWitt, D. P.; Bergman, T. L.; Lavine, A. S. *Fundamentals of Heat and Mass Transfer*, 6th ed.; John Wiley and Sons: New York, 2007.
(59) Schmidt, E.; Schurig, W.; Sellschopp, W. Versuche uber die Kondensation von Wasserdampf in Film und Tropfenform. *Forsch. Ingenieurwes.* **1930**, *1*, 53−63.
(60) Yun, R.; Heo, J.; Kim, Y. Effects of Surface Roughness and Tube Materials on the Filmwise Condensation Heat Transfer Coefficient at Low Heat Transfer Rates. *Int. Commun. Heat Mass Transfer* **2006**, *33*, 445−450.

DOI: 10.1021/acsami.5b06759
ACS Appl. Mater. Interfaces XXXX, XXX, XXX−XXX